

Beam Steering and Radiation Generation of Electrons in Bent Crystals in the Sub-GeV Domain

R. Negrello^{1,2}, M. Romagnoni^{1,2}, A. Sytov², N. Canale², D. De Salvador^{3,4}, P. Fedeli^{1,2}, V. Guidi^{1,2}, V. V. Haurylavets, P. Klag⁶, W. Lauth⁶, L. Malagutti², A. Mazzolari^{1,2}, G. Paternó², F. Sgarbossa^{3,4}, M. Soldani⁵, V. V. Tikhomirov, D. Valzani^{3,4}, L. Bandiera^{2*}

¹Department of Physics and Earth Science, University of Ferrara, Via Saragat 1, Ferrara, 44122, Italy.

²INFN, Via Saragat 1, Ferrara, 44122, Italy.

³Department of Physics, University of Padua, Via Marzolo 8, Padua, 35131, Italy.

⁴INFN Laboratori Nazionali di Legnaro, Viale dell'Università 2, Legnaro, 35020, Italy.

⁵INFN Laboratori Nazionali di Frascati, Via Enrico Fermi 54, Frascati, 00044, Italy.

⁶Institut für Kernphysik, Universität Mainz, Mainz, 55099, Germany.

*Corresponding author(s). E-mail(s): bandiera@fe.infn.it;

Abstract

We present an investigation into beam steering and radiation emission by sub-GeV electrons traversing bent silicon crystals. Using 855, 600, and 300 MeV electron beams at the Mainz Microtron (MAMI), we explored orientational coherent effects and particle dynamics in a 15 μm -thick crystal bent along the (111) planes. Combined experimental and simulation analyses enabled the classification and quantitative assessment of the contributions from channeling, dechanneling, rechanneling, and volume capture to both beam deflection and radiation emission. Crystal steering remained effective even at 300 MeV, with measured channeling efficiencies exceeding 50%, a record at such low energy. Channeling and volume reflection enhanced radiation emission by up to a factor of six compared to the misaligned orientation, highlighting strong orientational coherence effects in the sub-GeV regime. These findings confirm the feasibility of using bent crystals for efficient beam manipulation and high-intensity photon generation at low energies, supporting the development of novel light sources and beam control strategies at accelerator facilities operating in this energy range.

Keywords: Channeling, Crystals, Steering, Radiation

1 Introduction

Coherent interactions in crystals

Since the 1960s, it has been established that electrons and positrons traversing crystalline materials along specific lattice directions can

emit radiation far more intense than ordinary bremsstrahlung, as a result of coherent interactions with the crystal lattice [1, 2, 3]. This enhancement, first predicted by Ferretti [4] and Ter-Mikaelian [1] and later formalized by Dyson

and Überall [5], revealed the possibility of exploiting ordered atomic structures as sources of intense X-rays and γ rays [6].

The earliest observed manifestation of such coherence was *coherent bremsstrahlung* [1], experimentally demonstrated in 1960 by Diambri-Palazzi and collaborators at Frascati. It occurs when the momentum transferred from a relativistic electron (or positron) to the crystal matches a reciprocal-lattice vector, producing constructive interference in the emitted radiation.

From coherent bremsstrahlung to channeling

A few years later, the concept of *channeling* emerged from simulations of ion trajectories in oriented crystals [7]. When the incidence angle between the incoming charged particle and a major crystallographic plane or axis is smaller than the so-called Lindhard angle,

$$\vartheta_L = \sqrt{2U_0/E},$$

where U_0 is the potential-well depth and E the particle energy, the particle experiences correlated collisions with successive atomic rows or planes [8]. In this regime, the discrete atomic fields can be approximated by a continuous potential that confines the particle within the interplanar (or axial) well.

Typical potential depths range from a few tens of eV for planar channeling in silicon to several hundred eV along axial directions, and up to nearly 1 keV in high- Z crystals such as tungsten. Particles trapped in these potential wells undergo oscillatory motion, giving rise to *channeling radiation* [9], emitted within a narrow cone of semi-aperture $\sim \vartheta_L$, which scales as $E^{-1/2}$. Although typically softer than coherent bremsstrahlung, this radiation exhibits higher intensity due to the sustained coherence of the motion.

The efficiency of channeling radiation is limited by *dechanneling* [10, 11], the process by which incoherent scattering with electrons and nuclei ejects particles from the potential well. Particles that re-enter the well are said to undergo *rechanneling*. Both processes are driven by stochastic interactions with the lattice and play a central role in the overall steering and radiation dynamics.

Bent crystals and steering phenomena

The application of channeling to beam steering was proposed by Tsyganov in 1976 [12] and has since been extensively investigated at major accelerators including the LHC, Fermilab, and U-70 [13, 14, 15, 16]. In a bent crystal, the curvature of the atomic planes acts as a guiding structure, forcing channeled particles to follow the crystal's geometry.

Another coherent effect, *volume reflection* (VR), occurs when over-barrier particles are reflected by the curved potential barrier [17]. VR typically exhibits a larger angular acceptance than channeling and yields deflection angles on the order of ϑ_L .

Panel (a) of Fig. 1 shows the evolution of the bent-plane potential for the three investigated energies (300, 600, and 855 MeV), while panel (b) sketches the principal dynamical regimes within adjacent channels. As the energy decreases, the potential well deepens and widens, allowing a larger fraction of the beam to be trapped. Particles reflected at the potential barrier (red arrows) undergo VR deflection of order ϑ_L ; others may be captured after traversing a finite depth, a process referred to as *volume capture* or *capture over barrier*.

To visualize the mechanism that limits the steering efficiency, Fig. 2 depicts the concept of the *dechanneling length* $\langle L_d \rangle$ in a bent crystal. Particles initially captured in channeling oscillate along the bent planes until incoherent scattering drives them over the barrier. The average path length before escape defines $\langle L_d \rangle$, related to the *dechanneling angle* $\langle \vartheta_{\text{dech}} \rangle = \langle L_d \rangle / R_{\text{bending}}$.

Since volume reflection involves particles that do not experience dechanneling, it generally achieves higher deflection efficiencies than channeling, for both positively charged [18, 19] and negatively charged [20] particles.

Motivation for sub-GeV studies

While channeling and volume reflection have been thoroughly investigated from GeV to TeV energies [21, 22, 23], the sub-GeV regime remains comparatively unexplored [24, 25, 26, 27]. This energy range, hundreds of MeV to about 1 GeV, is particularly relevant for radiation applications, enabling intense hard X-ray (photon energies above ~ 10 keV) and γ -ray emission from compact

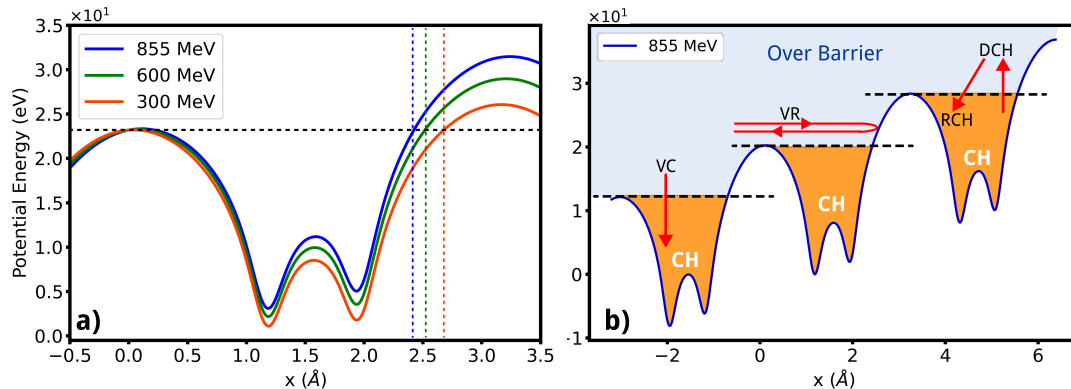


Fig. 1 (a) Potential energy of bent Si(111) planes for 300 (red), 600 (green), and 855 (blue) MeV electrons. The horizontal line at $x = 0$ indicates the reference potential, highlighting how the potential-well amplitude increases as the beam energy decreases. (b) Illustration of the main dynamical regimes experienced by charged particles: Over-barrier (OB), Volume Reflection (VR), Channeling (CH), Dechanneling (DCH), Rechanneling (RCH), and Volume Capture (VC).

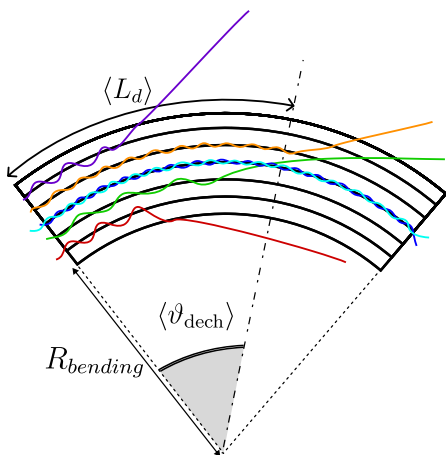


Fig. 2 Schematic representation of the dechanneling process in a bent crystal. Curved black lines: atomic planes; colored lines: representative particle trajectories. The mean dechanneling length $\langle L_d \rangle$ and the corresponding angle $\langle \vartheta_{\text{dech}} \rangle$ are related through the crystal curvature R_{bending} .

accelerators. Coherent effects in bent crystals at these energies promise efficient, cost-effective light sources for X-ray microscopy, industrial radiography, and advanced beam steering. Moreover, the lower energies facilitate the use of high- Z materials and low-emittance beams to enhance crystalline-radiation yields.

In this work, we investigate the interaction of sub-GeV electrons with bent silicon crystals, focusing on how beam steering and radiation generation evolve with beam energy. Combining experimental measurements and GEANT4-based simulations, we quantify the interplay between

channeling, dechanneling, and rechanneling mechanisms down to 300 MeV, an energy lying near the transition between the classical and quantum regimes of channeling, and directly relevant for next-generation compact LINAC facilities worldwide [28, 29].

2 Experimental setup

The experiment was carried out in Hall B of the Mainz Microtron (MAMI) using electron beams with energies of 855, 600, and 300 MeV. A schematic of the beamline and of the crystal geometry is shown in Fig. 3. After crossing the bent silicon crystal, the electrons entered a dipole magnet that deflected their trajectories by 44° . The magnet served to separate the charged beam from the forward-emitted radiation: electrons were bent toward the LYSO detector used for steering measurements, while photons proceeded along the beam axis toward the NaI(Tl) calorimeter.

The LYSO screen, $200 \mu\text{m}$ thick and imaged by a CCD camera, was positioned 6.02 m downstream of the magnet center, allowing the measurement of angular deflections with microradian precision. Beam monitoring was provided by an ionization chamber and a ZnS screen. A high-precision five-axis goniometer (three rotations and two translations) allowed the alignment of the crystal planes with respect to the incoming beam, which was focused by quadrupoles to an rms size of about $100 \mu\text{m}$ and an rms divergence of $30 \mu\text{rad}$. The

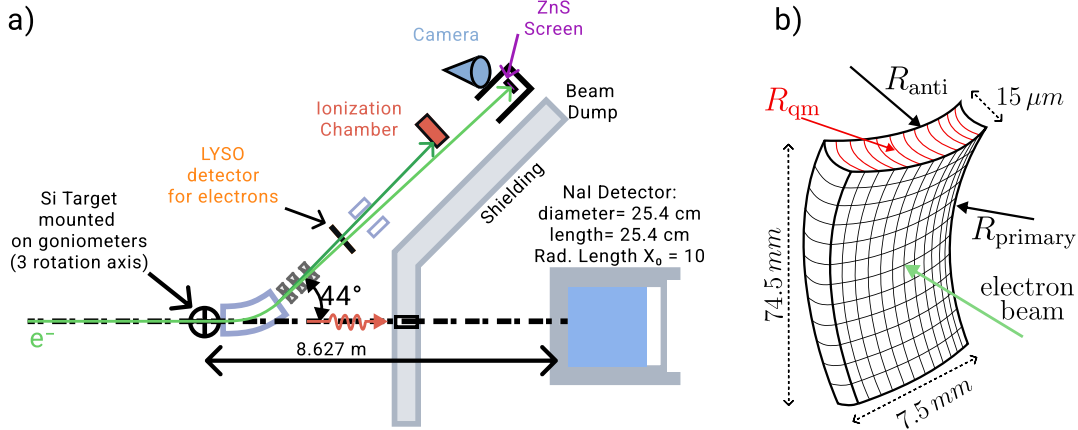


Fig. 3 (a) Scheme of the experimental setup at MAMI B, adapted from [26].(b) Geometry of the bent Si(111) crystal mounted on the holder that imparts the deformation

beam divergence was smaller than the Lindhard critical angle at all investigated energies.

The emitted radiation was collected by a thallium-doped sodium iodide (NaI(Tl)) crystal scintillator (25.4 cm diameter, 25.4 cm length, radiation length $X_0 = 10$) read out by three PMTs. A collimator with 40 mm aperture located 8.627 m downstream of the crystal defined an angular acceptance of 2.32 mrad, selecting photons emitted close to the forward direction.

The employed Si(111) crystal was a $15 \pm 1 \mu\text{m}$ -thick membrane with lateral dimensions of $74.5 \times 7.5 \text{ mm}^2$. The sample was mounted on a mechanical holder that imposed a primary curvature R_{primary} orthogonal to the (111) planes. Due to the elastic anisotropy of silicon, this external deformation induces a *quasi-mosaic* curvature R_{qm} along the (111) planes, the curvature actually experienced by the electrons and responsible for beam steering. In the following, we denote this effective curvature as $R_{\text{bending}} \equiv R_{\text{qm}}$. This phenomenon, known as the quasi-mosaic effect [30, 31], enables the controlled bending of thin crystalline membranes. A weaker anticlasic curvature R_{anti} develops in the orthogonal direction but is minimized by the chosen aspect ratio[32], resulting in an almost cylindrical surface in the central region of the crystal.

The nominal bending angle of the (111) planes is $\vartheta_b \simeq (450 \pm 5) \mu\text{rad}$, corresponding to an effective radius $R_{\text{qm}} \simeq \ell/\vartheta_b \approx 33.3 \text{ mm}$ for a crystal length of $15 \mu\text{m}$. The thickness was selected to be shorter than the dechanneling length at 855 MeV

(estimated to be $L_d \simeq 20 \mu\text{m}$) to preserve the channeling condition throughout the crystal. Since the beam spot was much smaller than the crystal surface, the entire beam intercepted the crystal; the relevant acceptance is therefore angular rather than geometric.

3 Beam Steering

Experimental and Simulated Deflection Profiles

The steering of charged particles in bent crystals arises from the collective action of interplanar electric fields, which guide the trajectories of particles initially captured in the channeling regime. To investigate this effect, we measured the deflection efficiency as a function of beam energy and compared the results with dedicated GEANT4-based simulations performed under identical conditions.

Experimentally, the angular distribution of particles emerging from the crystal was recorded as a function of the incidence angle α between the beam direction and the crystallographic (111) planes (the so-called *goniometer angle*). Simulations were carried out in parallel using the G4CHANNELINGFASTSIMMODEL [33], a module that embeds the physics of planar channeling, dechanneling, and rechanneling directly within the GEANT4 framework [34, 35, 36]. This approach reproduces the experimental geometry, beam divergence, and bending radius, enabling a one-to-one comparison between simulated and measured distributions. The simulation procedure follows

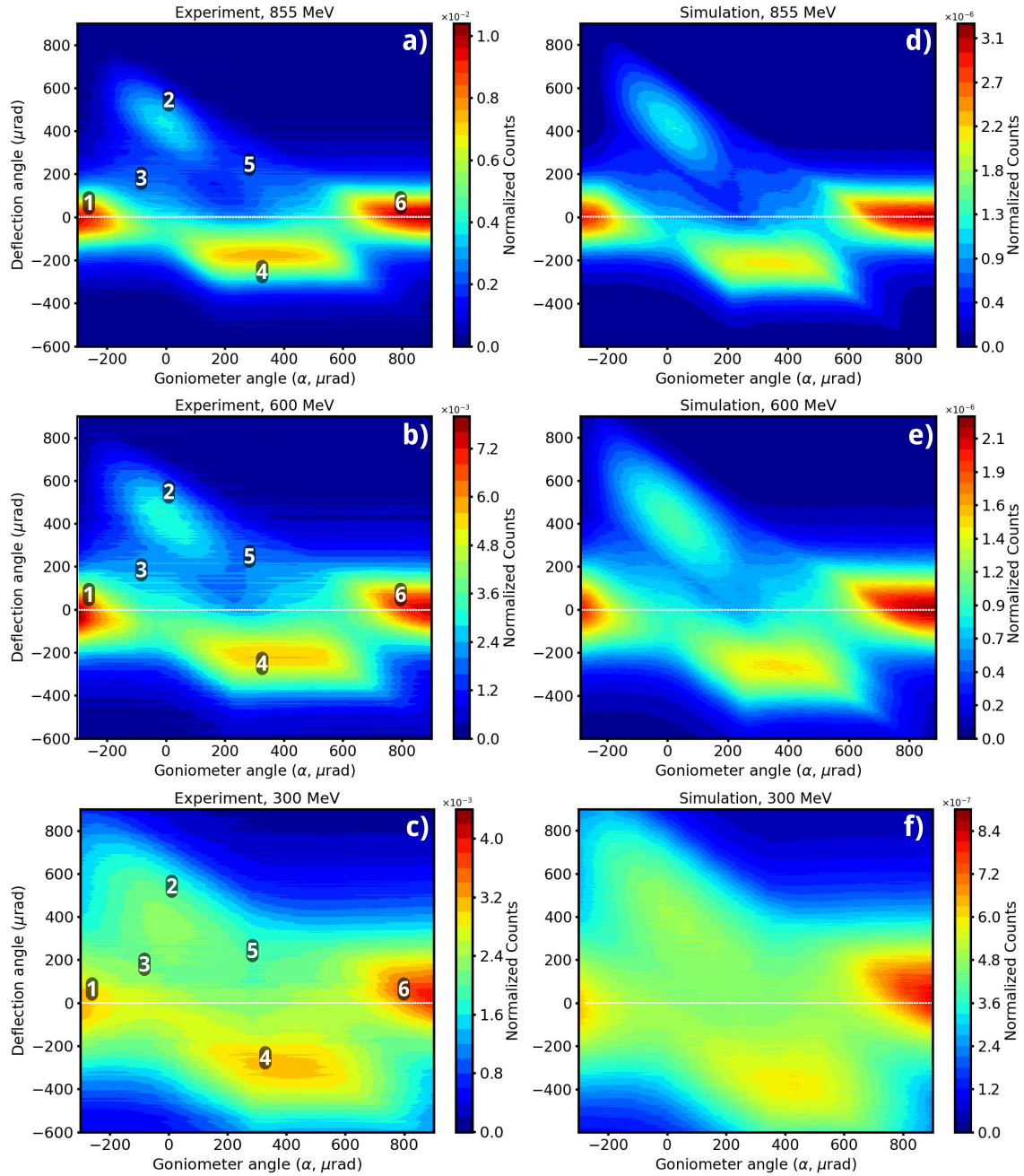


Fig. 4 Experimental (a–c) and simulated (d–f) angular scans at the investigated energies. Six regions can be distinguished: (1)–(6) amorphous, (2) channeling, (3) dechanneling, (4) volume reflection, and (5) volume capture.

the methodology established in previous research works [23, 21, 37, 38, 39], and its trajectory-level analysis is described in detail in Sec. 3.

Figure 4 displays the measured (a–c) and simulated (d–f) angular scans at the investigated energies. Six distinct regions can be identified: (1)

and (6) amorphous orientations, (2) channeling deflection, (3) dechanneling, (4) volume reflection, and (5) volume capture. Simulated angular scans closely reproduce the experimental observations across all energies, confirming the accurate modeling of the beam–crystal interaction dynamics.

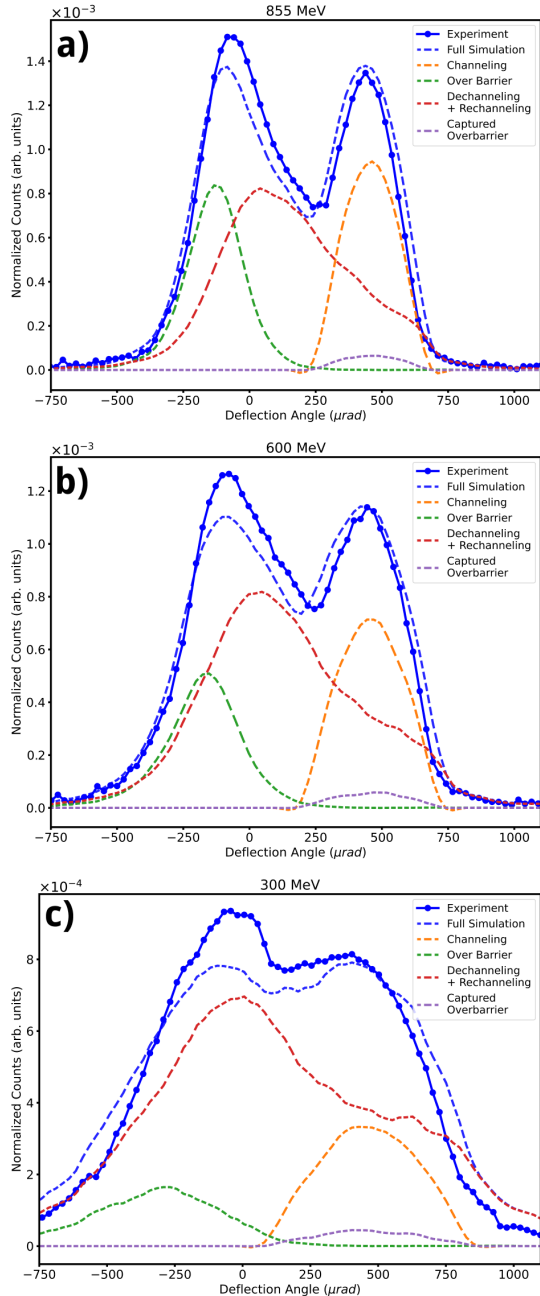


Fig. 5 Profiles of the deflected beam under channeling conditions. Experimental data (solid blue) are compared with simulated distributions (dashed), whose sub-components correspond to distinct mechanisms within the bent crystal. The contribution labeled “dechanneling + rechanneling” includes all trajectories that underwent at least one dechanneling event.

When the crystal is aligned with the channeling condition ($\alpha \approx 0$), the deflection profile exhibits two main peaks corresponding to channeling and

volume reflection. Figure 5 compares the experimental distributions (solid blue lines with markers) with the simulated curves (dashed lines). Each simulated sub-distribution (colored dashed lines) is derived from the trajectory-level classification of simulated particles into distinct dynamical states: channeled, dechanneled/rechanneled, over-barrier, and captured over-barrier, as detailed in the following subsec. 3. The comparison reveals very good agreement at 855 MeV and 600 MeV, and reasonable agreement at 300 MeV, where multiple scattering and a larger critical angle broaden the distributions. This decomposition provides a direct physical interpretation of the measured deflection profiles, illustrating how the different interaction mechanisms collectively shape the overall angular distribution.

As the beam energy decreases, the broadening of the peaks becomes more pronounced. This arises from two concurrent effects: enhanced multiple scattering at lower energies, which increases the angular spread of the volume-reflected component, and the increase of the Lindhard critical angle ϑ_L , which enlarges the channeling acceptance and consequently the width of the channeled peak. Both effects are particularly evident at 300 MeV, where scattering and the larger ϑ_L combine to produce a broad, partially overlapping distribution.

The channeling efficiency η , defined as the ratio between the number of particles deflected within 3σ of the channeling peak and the total number of detected events, was extracted from Gaussian fits to the deflection profiles. From the same fits, the mean deflection angle was obtained as $445 \pm 5 \mu\text{rad}$, a value consistent across all investigated energies and used for the subsequent evaluation of the crystal bending radius. Table 1 summarizes the measured and simulated efficiencies, together with the relevant crystal parameters: the bending radius R_{bending} , the critical radius $R_C = pv/E_0$, and the Lindhard angle ϑ_L . Despite the expected enhancement of dechanneling at lower energies, the channeling efficiency rises from 39% to 54% as the beam energy decreases. This counter-intuitive trend is explained by the larger ratio R_{bending}/R_C , which effectively broadens the potential well and increases the phase-space region available for stable channeling.

Table 1 Experimental and simulated deflection efficiencies. R_{bending} is the bending radius of the crystal, R_C the critical radius, and ϑ_L the Lindhard angle.

Energy [MeV]	R_{bending}/R_C	ϑ_L [μrad]	η_{exp} [%]	η_{sim} [%]
855	22	200.5	39 ± 2	44 ± 2
600	31.5	243.1	45 ± 4	49 ± 3
300	62.4	349.1	54 ± 5	61 ± 4

These results demonstrate that both experiment and simulations capture the same underlying trends in beam steering efficiency. To quantify these observations and to isolate the effects of dechanneling and rechanneling, a detailed analysis was carried out, as discussed in the following subsection.

Quantitative Analysis of Channeling and Dechanneling

To extract the characteristic parameters governing beam steering, the angular distributions were

$$\frac{df_{ch}}{d\vartheta} = \frac{A_{ch}}{\sigma_{ch}\sqrt{2\pi}} \exp\left[-\frac{(\vartheta - \vartheta_{ch})^2}{2\sigma_{ch}^2}\right], \quad (1)$$

$$\frac{df_{VR}}{d\vartheta} = \frac{A_{VR}}{\sigma_{VR}\sqrt{2\pi}} \exp\left[-\frac{(\vartheta - \vartheta_{VR})^2}{2\sigma_{VR}^2}\right] + \frac{1 - A_{VR}}{r\sigma_{VR}\sqrt{2\pi}} \exp\left[-\frac{(\vartheta - \vartheta_{VR})^2}{2r^2\sigma_{VR}^2}\right], \quad (2)$$

$$\begin{aligned} \frac{df_{dech}}{d\vartheta} = & \frac{A_{dech}}{2\vartheta_{dech}} \exp\left[-\frac{\sigma_{VR}^2}{2\vartheta_{dech}^2} + \frac{\vartheta_{ch} - \vartheta}{\vartheta_{dech}}\right] \\ & \times \left\{ \text{erf}\left(\frac{\vartheta_{VR} - \vartheta + \sigma_{VR}^2/\vartheta_{dech}}{\sqrt{2}\sigma_{VR}}\right) - \text{erf}\left(\frac{\vartheta_{ch} - \vartheta + \sigma_{VR}^2/\vartheta_{dech}}{\sqrt{2}\sigma_{VR}}\right) \right\}, \quad (3) \end{aligned}$$

$$\frac{1}{N} \frac{dN}{d\vartheta} = \frac{df_{ch}}{d\vartheta} + B_{VR} \frac{df_{VR}}{d\vartheta} + \frac{df_{dech}}{d\vartheta}. \quad (4)$$

In Eqs. (1)–(4), the amplitudes A_{ch} , A_{VR} , A_{dech} , B_{VR} , and the ratio r are normalization parameters. The angles ϑ_{ch} and ϑ_{VR} , together with their corresponding widths σ_{ch} and σ_{VR} , define the mean positions and standard deviations of the channeling and volume-reflection peaks. The parameter ϑ_{dech} represents the *dechanneling angle*, which defines the dechanneling length through $L_d = \vartheta_{dech} R_{\text{bending}}$.

The fit procedure was performed in two stages. First, Eq. (2) was applied to the angular distribution measured with the crystal in an amorphous

orientation to determine the reference parameters A_{VR} and r . These values were then fixed in the global fit (4) of the oriented data, while all other parameters were left free within physically reasonable bounds. From this global fitting procedure, the dechanneling lengths $L_{d,\text{exp fit}}$ and $L_{d,\text{sim fit}}$ were obtained for the experimental and simulated angular distributions, respectively. These values, reported in the first two columns of Table 2, represent the results derived directly from the analytical modeling of the measured and simulated deflection profiles. The remaining columns ($L_{d,\text{with rech}}$ and $L_{d,\text{without rech}}$) correspond instead to dechanneling lengths extracted

Table 2 Experimental and simulated dechanneling lengths, with and without rechanneling (rech).

Energy [MeV]	R_{bending}/R_C	$L_{d,\text{exp fit}} [\mu\text{m}]$	$L_{d,\text{sim fit}} [\mu\text{m}]$	$L_{d,\text{with rech}} [\mu\text{m}]$	$L_{d,\text{without rech}} [\mu\text{m}]$
855	22	20 ± 2	21 ± 4	21 ± 2	16 ± 1
600	31.5	15 ± 2	14 ± 3	15 ± 1	13 ± 1
300	62.4	–	–	9.5 ± 0.4	9.4 ± 0.3

from a complementary, purely simulation-based approach described later in this section, in which crystals of varying thickness were simulated at fixed R_{bending}/R_C . The agreement between the fitted and simulated values, as well as with previous measurements [21, 23], confirms the consistency and robustness of the overall analysis methodology.

For the 300 MeV case, the experimental angular distribution did not exhibit a well-isolated channeling peak because of the strong overlap between channeling and volume-reflection regions and the broadening induced by the larger Lindhard angle. For this reason, no reliable fit could be performed, and the dechanneling length at 300 MeV was instead extracted from the simulation-based thickness-dependence method described later in this section.

In addition to the analytical fits, a dedicated trajectory-tagging code was developed to analyze GEANT4 simulations at a microscopic level and to identify the dynamical state of each particle along its path. The method described in Ref. [40], extends the approach of Ref. [23] by including additional physical effects relevant to bent crystals. Each simulated trajectory was discretized into segments of tens of nanometers. For each segment, the transverse energy E_T was compared to the potential barrier U_0 : segments were classified as *channeled* if $E_T < U_0$ and *over-barrier* otherwise. The sequence of states within each trajectory was then used to categorize the particle behavior into the following classes:

- **Channeling:** particle remains in the channeled state for the entire trajectory;
- **Over-barrier:** particle remains over-barrier throughout the trajectory;
- **Dechanneling:** transition from an initial channeled state to an over-barrier state;
- **Rechanneling:** repeated transitions between channeled and over-barrier states;

- **Captured over-barrier:** transition from an over-barrier to a channeled state persisting until the crystal exit.

This methodology enables the decomposition of the deflected particle distribution into distinct contributions from the various beam–crystal interaction mechanisms, as shown in Fig. 5. By analyzing these components, it is possible to identify the principal factors shaping the overall deflection profile. As the beam energy decreases from 855 MeV to 300 MeV, the width of the channeling distribution (green dashed lines) broadens owing to the increase in the critical angle ϑ_L . Simultaneously, the fraction of purely over-barrier particles (red dashed lines) decreases, while the proportion of trajectories experiencing at least one dechanneling event (purple dashed lines) grows. At 300 MeV, the deflected peak is predominantly formed by particles undergoing multiple rechanneling episodes, underscoring the key role of this process in sustaining beam steering at low energy.

The same analysis allows distinguishing between the overall deflection angle and the *channeling-only* deflection angle. Gaussian fits to the full angular distribution yield a mean deflection of $445 \pm 5 \mu\text{rad}$ for both experimental and simulated data, corresponding to an effective bending radius $R = (33.7 \pm 2.3) \text{ mm}$. When the fit is restricted to the channeling component alone (green dashed curve in Fig. 5), the peak shifts to $460 \pm 5 \mu\text{rad}$, corresponding to the actual crystal bending angle. The corresponding radius, $R_{\text{bending}} = (32.6 \pm 2.2) \text{ mm}$, highlights that the global deflection angle includes contributions from all coherent interactions within the bent crystal, with dechanneling producing a measurable reduction.

To further quantify dechanneling, an independent method inspired by Ref. [23] was employed. Simulations of bent crystals with varying lengths

were performed while maintaining a constant curvature ratio R_{bending}/R_C . The number of channeled particles at the crystal exit, $N_{\text{ch}}(\ell)$, was fitted with an exponential decay:

$$N_{\text{ch}}(\ell) = N_0 \exp(-\ell/L_d)$$

yielding dechanneling lengths L_d of 21 μm at 855 MeV, 14 μm at 600 MeV, and 9.4 μm at 300 MeV. These values include the effect of rechanneling and are consistent with those obtained from the global fits. When only initially channeled particles are considered, the corresponding L_d values reduce to 16 μm , 13 μm , and 9.3 μm , respectively, demonstrating the significant role of rechanneling in extending the effective dechanneling length and maintaining high steering efficiency in the sub-GeV regime.

4 Radiation Generation

The emission of electromagnetic radiation by sub-GeV electrons traversing bent silicon crystals is the natural radiative counterpart of the coherent orientational effects discussed in Sec. 3. While Sec. 3 focused on steering and dechanneling dynamics, here we quantify how those mechanisms translate into measurable photon emission as a function of energy and orientation, combining experimental measurements and GEANT4-based simulations.

Experimental Setup and Simulation Methodology

The experimental geometry and the crystal are the same as described in the setup section and used for the deflection study (see Sec. 3); here we recall only the elements specific to the radiation measurement. The NaI(Tl) detector was placed at $L = 8.627$ m and equipped with a circular collimator of diameter 40 mm, corresponding to a half-aperture $\vartheta_{\text{det}} \simeq 2.32$ mrad, which fully encompasses the forward emission cone (of order $1/\gamma$): for 300, 600, and 855 MeV, $1/\gamma = 1.70, 0.85,$ and 0.60 mrad, i.e. the acceptance corresponds to $\sim 1.4, \sim 2.7,$ and ~ 3.9 times $1/\gamma$, respectively.

Radiation spectra were acquired versus the beam-to-plane angle α with four characteristic orientations:

- Channeling (CH): $\alpha \approx 0,$

- Volume Reflection (VR): $\alpha \approx +314\text{--}340$ $\mu\text{rad},$
- Anti-Volume Reflection (AVR): $\alpha \approx -314\text{--}340$ $\mu\text{rad},$
- Random (amorphous-like): $\alpha > 10$ mrad, i.e., well beyond any planar or axial alignment, so that residual coherent contributions are negligible within our angular resolution.

Here *anti-volume reflection* denotes the configuration on the side opposite to VR, at $|\alpha|$ slightly larger than the Lindhard angle, where particles approach the bent-plane barrier from the opposite sign of α ; it can be viewed as a CB-like entrance condition mirrored with respect to VR. Each spectrum was background-corrected and normalized. Following [41], we plot the spectral intensities as $E_\gamma dN/dE_\gamma$.

Simulations were performed with `G4ChannelingFastSimModel` [33] in GEANT4 [34, 36], reproducing beam divergence, crystal curvature, and detector acceptance. For each (energy, orientation) configuration we simulated 10^7 electrons. Statistical uncertainties are below 10^{-6} and negligible at the plot scale ($\sim 10^{-3}$). The custom Python-based tagging tool [40], used for the previous section can be used to associate each emitted photon to the dynamical regime of the emitting particle.

Experimental Results and Comparison with Simulations

Figure 6 shows the measured and simulated spectra. A pronounced peak is observed in channeling (blue), while VR (dark orange) and AVR (green) yield weaker but clearly coherent emission; random orientations (red) reproduce the amorphous baseline. Across 0.2–8 MeV the coherent spectra exceed the amorphous level. Enhancement factors, relative to the amorphous condition, are ~ 6.3 (CH) and ~ 5.0 (VR) at 855 MeV; ~ 6.7 and ~ 4.6 at 600 MeV; and ~ 5.6 and ~ 3.6 at 300 MeV.

The channeling peak follows [42]:

$$\hbar\omega = \frac{4\hbar c}{d_p} \sqrt{\frac{2U_0}{m}} \gamma^{3/2}, \quad (5)$$

with $d_p = 2.35$ \AA (Si(111)) and $U_0 = 21$ eV. Table 3 shows the excellent agreement among theory, data, and simulations. Simulations reproduce the spectra very well at 855 and 600 MeV and

Table 3 Main channeling-harmonic peak: theory vs experiment and simulation.

Energy [MeV]	R_{bending}/R_C	$E_{\text{peak}}^{\text{theory}}$ [MeV]	$E_{\text{peak}}^{\text{exp}}$ [MeV]	$E_{\text{peak}}^{\text{sim}}$ [MeV]
855	21.6	1.9	1.8 ± 0.2	1.9 ± 0.1
600	30.8	1.2	1.1 ± 0.2	1.2 ± 0.1
300	61.5	0.43	0.46 ± 0.08	0.43 ± 0.05

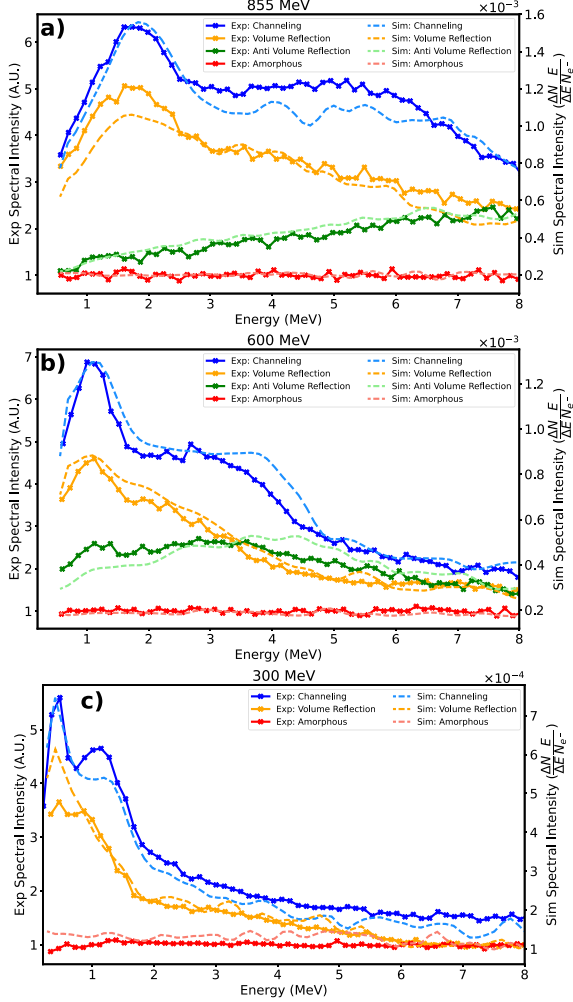


Fig. 6 Experimental (solid) and simulated (dashed) radiation spectral intensities for different energies and orientations. Blue: channeling; dark orange: VR; green: AVR; red: random orientation. Intensities in arbitrary units (arb. units).

satisfactorily at 300 MeV, where larger multiple scattering and ϑ_L broaden the features.

Correlation between Particle Dynamics and Radiation Emission

Figure 7 displays the simulated spectral intensity distributions for the channeling configuration at beam energies of 855 MeV (top), 600 MeV (middle), and 300 MeV (bottom). The solid blue line shows the full simulation, while dashed lines represent the contributions from the five dynamical categories studied in this work: channeling (green), dechanneling + rechanneling (purple), over-barrier motion (red), and captured over-barrier (brown), as defined in the beam steering analysis (Sec. 3). In this representation, the contribution of dechanneling and rechanneling has been grouped together, as these two regimes are dynamically linked through multiple transitions. The associated percentage annotated in the figure indicates the relative share of rechanneling photons within the combined dechanneling + rechanneling signal, enabling a more accurate interpretation of their respective roles in the radiation process.

The classification of photon-emitting particles into these categories was achieved using a custom Python-based algorithm to analyze the simulation obtained with the Geant4 model, which associates each emitted photon to the dynamic phenomenon obtained by the classification of the complete trajectory of the emitting particle. This approach enables a direct correlation between particle dynamics and radiation generation, linking dynamical behavior with measurable radiation features [40].

Notably, the dechanneling contribution is dominant across all energies. As reported in Table 4, the fraction of photon-emitting particles identified as dechanneling increases from 46.28% at 855 MeV to 60.86% at 300 MeV. This trend is attributed to the enhanced multiple scattering at lower energies, which increases the likelihood of particles escaping the channeling regime. At the same time, the channeling regime is more populated due to the broader channeling critical angle ϑ_L , which defines the angular acceptance of the phenomenon.

Table 4 Fraction of particles emitting at least one photon and radiation efficiency for different particle dynamics categories and beam energies, for photon energy range [0, 8] MeV.

Beam Energy [MeV]	Category	Fraction over emitting (%)	Radiation efficiency (%)
855	Channeling	34.13	0.49
	Over Barrier	9.33	0.15
	Dechanneling	46.28	0.38
	Rechanneling	7.34	0.47
	Captured Over Barrier	2.92	0.47
600	Channeling	30.50	0.42
	Over Barrier	7.33	0.14
	Dechanneling	50.01	0.31
	Rechanneling	9.44	0.39
	Captured Over Barrier	2.72	0.36
300	Channeling	19.56	0.23
	Over Barrier	4.24	0.09
	Dechanneling	60.86	0.18
	Rechanneling	13.16	0.18
	Captured Over Barrier	2.19	0.18

Conversely, the contribution from particles remaining in channeling decreases with energy, from 34.13% (855 MeV) to 19.56% (300 MeV), due to increased scattering. The over-barrier fraction also diminishes (from 9.33% to 4.24%) as more particles enter bound states thanks to the increasing ϑ_L at lower energies. Interestingly, the rechanneling contribution increases from 7.34% to 13.16% as energy decreases. This suggests that particles undergo more frequent transitions between over-barrier and channeling states at lower energies. However, the captured over-barrier contribution, representing transitions from unbound to bound motion, slightly decreases from 2.92% at 855 MeV to 2.19% at 300 MeV, indicating reduced effectiveness of capture processes at low energies.

Across all beam energies, the contributions involving particles in channeling, whether directly or via rechanneling or capture, show a marked increase near the spectral peak. This underlines the central role of channeling oscillations in shaping the peak structure of the emitted radiation.

The "radiation efficiency" reported in Table 4 is defined, for each dynamical category, as the ratio between the number of particles that emitted at least one photon and the total number of particles assigned to that category. This quantity reflects the intrinsic emission probability within each dynamic regime and provides insights that

are complementary to the fraction over emitting. For channeling and rechanneling, the radiation efficiencies remain remarkably high and nearly constant across energies, with values ranging from 0.23% to 0.49%. This confirms that once a particle enters or reenters the channeling regime, the probability of radiation is substantial, and the underlying emission mechanism is robust even at low energy.

On the other hand, particles undergoing over-barrier motion show consistently low efficiencies, dropping from 0.15% at 855 MeV to 0.09% at 300 MeV. This reflects the absence of periodic potential confinement and the less coherent nature of their motion, which results in a reduced probability of significant photon emission. Similarly, the dechanneling category, although responsible for the largest fraction of emitting particles, exhibits moderate radiation efficiencies (from 0.38% to 0.18%), indicating that while many particles enter this regime, the probability of effective radiation per particle is not maximized. The captured over-barrier regime, which relies on the transition from unbound to bound states, also shows relatively high efficiencies (up to 0.47% at 855 MeV), suggesting that once capture occurs, the resulting emission resembles that of regular channeling, despite its low population fraction.

The increasing contribution from particles undergoing dechanneling and rechanneling with

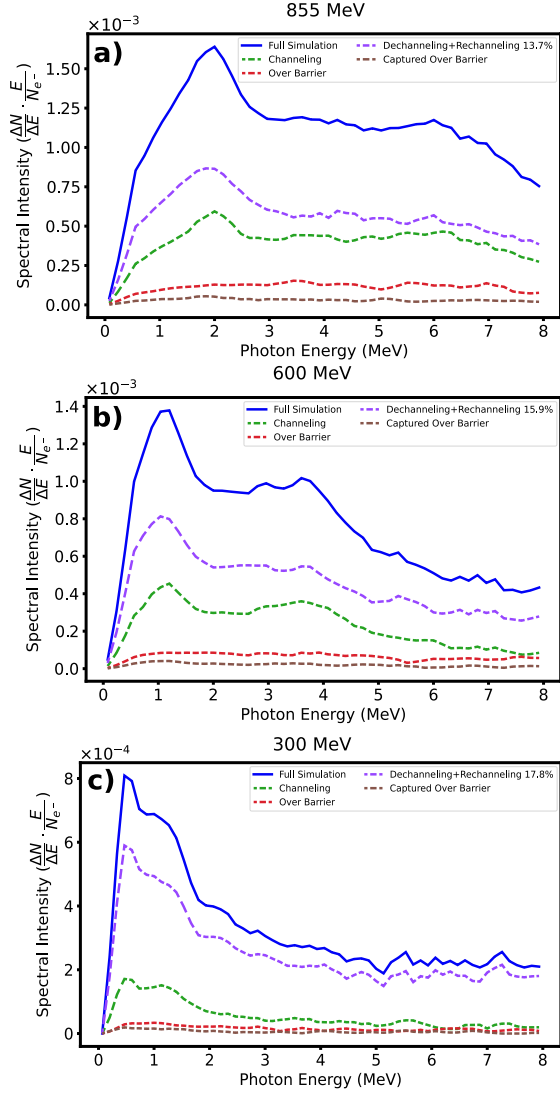


Fig. 7 Simulated spectral intensity $I(E_\gamma) = (\Delta N E_\gamma) / (\Delta E_\gamma N_{e^-})$ for 855, 600, and 300 MeV electrons under channeling conditions. Solid blue line: total simulated spectrum; dashed curves: contributions from channeling (green), dechanneling + rechanneling (purple), over-barrier (red), and captured over-barrier (brown) particles. Percentages in the legends indicate the fraction of photons emitted during rechanneling within the combined dechanneling + rechanneling signal. The growing prominence of these components at lower energy reflects enhanced multiple scattering and reduced stability of bound motion.

decreasing energy closely mirrors the trends observed in the beam-deflection analysis of Sec. 3, confirming the common dynamical origin of both effects.

Efficiency Scaling and Crystal Optimization

To relate the observed efficiencies to the crystal thickness ℓ and the dechanneling length L_d , we use the exponential saturation model:

$$\varepsilon_{ch}(\ell) = \varepsilon_{ch}^{\max} \left(1 - e^{-\ell/L_d} \right), \quad (6)$$

with L_d from Table 2 (21, 14, and 9.4 μm at 855, 600, and 300 MeV). Using the simulated efficiencies for $\ell = 15 \mu\text{m}$ (0.49%, 0.42%, 0.23%), we obtain

$$\varepsilon_{ch}^{\max} = 0.96\%, 0.63\%, 0.29\%,$$

and the thicknesses for 90% saturation equal to 48.4, 32.2, and 21.6 μm , respectively.

These findings indicate that the 15 μm crystal is nearly optimal for the 300 MeV beam, capturing about 78% of the maximum possible channeling radiation, while at 600 MeV and 855 MeV, the capture is limited to 63% and 51%, respectively. Therefore, for higher energies, a longer crystal would improve the emission yield significantly. This analysis, while focused on channeling, also underscores the contrasting behavior of other categories: for instance, increasing crystal length would likely not improve the low efficiency observed in the over-barrier regime. These conclusions contribute to the rational design of advanced crystal-based radiation sources, where the balance between crystal length, energy loss, and photon yield must be optimized to meet stringent application requirements in accelerator-based light sources.

5 Discussion and Conclusions

In this work, we have presented a comprehensive experimental and numerical investigation of beam steering and radiation generation by sub-GeV electrons in bent silicon crystals. By systematically exploring the energy range of 300–855 MeV, we have extended the study of coherent effects well below the GeV scale and introduced a new interpretative framework in which radiation is directly linked to particle dynamics within the crystal. The combined analysis of deflection profiles and

radiation spectra—supported by trajectory classification in simulations—provides a direct correlation between steering mechanisms and their radiative signatures, clarifying how microscopic motion governs both emission efficiency and spectral characteristics.

Steering and radiation dynamics.

Deflection measurements confirm that bent-crystal steering remains remarkably effective down to 300 MeV, with experimental channeling efficiencies increasing from 39% at 855 MeV to 54% at 300 MeV—a record value at this energy [22]. This trend, supported by simulations, originates from the increased ratio R_{bending}/R_C , which enlarges the phase space for stable channeling. The extracted dechanneling lengths and the trajectory-level analysis reveal that rechanneling becomes dominant at 300 MeV, compensating for stronger multiple scattering and shorter L_d . Radiation spectra measured under channeling and volume-reflection conditions show enhancements up to a factor of six compared with the amorphous case, with the photon-energy peak shifting from ~ 1.8 MeV at 855 MeV to ~ 0.46 MeV at 300 MeV. The agreement between experiment, simulation, and theory confirms the coherent nature of the emission. Simulations indicate that, as energy decreases, dechanneling and rechanneling processes dominate the radiative output: the fraction of photons emitted during dechanneling rises from 46.3% at 855 MeV to 60.8% at 300 MeV, while the contribution of stably channeled particles decreases from 34.1% to 19.6%. This behavior reflects the enhanced role of multiple scattering and the reduced coherence length at low energy.

Emission efficiency

The radiation efficiency, defined as the probability of emitting at least one photon within a given dynamical regime, provides deeper insight into these mechanisms. Channeling trajectories exhibit the highest efficiencies at all energies (0.49% at 855 MeV, 0.23% at 300 MeV), while rechanneling and captured-over-barrier particles show comparable values up to 0.47%. Once a particle is re-trapped into the potential well, its emission probability becomes nearly identical to that of a stably channeled particle. Over-barrier particles exhibit the lowest efficiencies (0.15–0.09%), as expected

for non-periodic motion, while dechanneling trajectories, though numerous, show moderate values (0.38–0.18%). These results quantitatively link radiation yield to the dynamics and demonstrate that transient channeling states significantly sustain the total emission at low energy. Moreover, the saturation model applied to the channeling efficiency indicates that thicker crystals could substantially increase the yield, especially at higher energies where the present 15 μm thickness is below the asymptotic optimum.

Applications and outlook

This study provides the first experimental evidence of enhanced radiation from bent silicon crystals at electron energies as low as 300 MeV. Even in this sub-GeV range, both channeling and volume reflection yield radiation intensities several times higher than in the random orientation—factors of six and four, respectively, at 300 MeV. Such performance confirms the feasibility of using bent crystals for beam steering and radiation generation in compact accelerators where conventional magnetic elements are impractical. The broader critical angle at low energy relaxes alignment tolerances, enhancing operational flexibility. Many facilities operate in the same range—MAMI, SAGA (255 MeV) [22], CLARA (250 MeV) [43], CLEAR@CERN (230 MeV) [44], ARES@DESY (160 MeV) [45], and SPARC LAB@INFN-LNF (180 MeV) [46]—and could benefit from these findings. At even lower energies (~ 100 MeV), channeling photons in the 60–80 keV range could serve X-ray microscopy [47] and industrial radiography [48]. The demonstrated ability to tune emission through crystal curvature and beam energy underscores the versatility of bent crystals as compact, tunable light sources. Volume reflection, less sensitive to crystal defects, remains efficient even for low-quality beams and high- Z materials such as tungsten [49, 50, 19, 24]. Finally, the trajectory-classification algorithm developed here provides a quantitative framework for designing advanced radiation sources based on periodically bent crystals (undulators) [51, 52, 53, 54, 55] and multi-volume-reflection systems [56, 57, 58, 59].

Overall, the combined experimental and simulation-based analysis presented here establishes a direct link between microscopic dynamics

and macroscopic radiation yield, paving the way for compact, high-efficiency γ -ray sources based on crystal-assisted mechanisms.

Funding

This work was supported by the European Commission through the H2020-MSCA-RISE N-LIGHT (Grant Agreement No. 872196), EIC-PATHFINDER-OPEN TECHNO-CLS (Grant Agreement No. 101046458), and INFN CSN5 (OREO and GEANT4INFN projects).

L. Malagutti acknowledges support from the MHz-TOMOSCOPY project (Grant Agreement No. 101046448).

A. Sytov acknowledges support from the H2020-MSCA-IF-Global TRILLION project (Grant Agreement No. 101032975).

N. Canale acknowledges support from the European Union – NextGenerationEU under the project "Intense positron source Based On Oriented crystals - e+BOOST" (Grant No. 2022Y87K7X, CUP I53D23001510006).

References

- [1] M. L. Ter-Mikaelian. *High-energy Electromagnetic Processes in Condensed Media*. Wiley, New York, 1972.
- [2] V. N. Baier, V. M. Katkov, and V. M. Strakhovenko. *Electromagnetic Processes at High Energies in Oriented Single Crystals*. World Scientific, Singapore, 1998.
- [3] A. I. Akhiezer and N. F. Shulga. *High-energy Electrodynamics in Matter*. Gordon and Breach, New York, 1996.
- [4] B. Ferretti. Sulla bremsstrahlung nei cristalli. *Nuovo Cimento*, 7:118, 1950.
- [5] H. Überall. High-energy interference effect of bremsstrahlung and pair production in crystals. *Phys. Rev.*, 103:1055, 1956.
- [6] H. Bilokon, G. Bologna, F. Celani, B.D'Ettorre Piazzoli, R. Falcioni, G. Mannocchi, and P. Picchi. Coherent bremsstrahlung in crystals as a tool for producing high energy photon beams to be used in photoproduction experiments at cern sps. *Nuclear Instruments and Methods in Physics Research*, 204(2):299–310, 1983.
- [7] Mark T. Robinson and O. S. Oen. The channeling of energetic atoms in crystal lattices. *Applied Physics Letters*, 2(2):30–32, 1963.
- [8] Jens Lindhard. Influence of crystal lattice on motion of energetic charged particles. *Mat. Fys. Medd. Dan. Vid. Selsk*, 34:1–65, 1965.
- [9] M. A. Kumakhov. On the theory of electromagnetic radiation of charged particles in a crystal. *Phys. Lett. A*, 57(1):17 – 18, 1976.
- [10] V. V. Beloshitsky, M. A. Kumakhov, and V. A. Muralev. Multiple scattering of channeling ions in crystals-ii. planar channeling. *Radiat. Eff*, 20:95–109, 1973.
- [11] R. P. Fliller III et al. Rhic crystal collimation. *Nucl. Instrum. Methods Phys. Res., Sect. B*, 234(12):47–56, 2005.
- [12] A. M. Tarantin, E. N. Tsyganov, and S. A. Vorobiev. Computer simulation of deflection effects for relativistic charged particles in a curved crystal. *Physics Letters A*, 72(2):145–146, 1979.
- [13] W. Scandale et al. Observation of channeling for 6500 gev/c protons in the crystal assisted collimation setup for lhc. *Physics Letters B*, 758:129–133, 2016.
- [14] R. A. Carrigan et al. Beam extraction studies at 900 gev using a channeling crystal. *Phys. Rev. ST Accel. Beams*, 5:043501, 2002.

- [15] D. Lietti et al. Radiation emission phenomena in bent silicon crystals: Theoretical and experimental studies with 120 gev/c positrons. *Nucl. Instrum. Methods Phys. Res. B*, 283:84–92, 2012.
- [16] W. Scandale et al. Optimization of the crystal assisted collimation of the sps beam. *Physics Letters B*, 726(1-3):182–186, 2013.
- [17] A. M. Taratin and S. A. Vorobiev. ”volume reflection” of high-energy charged particles in quasi-channeling states in bent crystals. *Phys. Lett. A*, 119(8):425–428, 1987.
- [18] W. Scandale et al. High-efficiency volume reflection of an ultrarelativistic proton beam with a bent silicon crystal. *Phys. Rev. Lett.*, 98:154801, 2007.
- [19] E. Bagli et al. Steering efficiency of an ultrarelativistic proton beam in a thin bent crystal. *Eur. Phys. J. C*, 74(1):2740, 2014.
- [20] W. Scandale et al. Observation of channeling and volume reflection in bent crystals for high-energy negative particles. *Phys. Lett. B*, 681(3):233–236, 2009.
- [21] A. I. Sytov et al. Steering of sub-gev electrons by ultrashort si and ge bent crystals. *Eur. Phys. J. C*, 77(12), 2017.
- [22] Y. Takabayashi, Yu.L. Pivovarov, and T.A. Tukhfatullin. Bent crystal channeling of 255 mev electrons. *Physics Letters A*, 382(4):153–156, 2018.
- [23] A. Mazzolari et al. Steering of a sub-gev electron beam through planar channeling enhanced by rechanneling. *Phys. Rev. Lett.*, 112:135503, 2014.
- [24] L. Bandiera et al. Investigation of the electromagnetic radiation emitted by sub-gev electrons in a bent crystal. *Phys. Rev. Lett.*, 115(2), 2015.
- [25] Alexander V. Pavlov, Andrei V. Korol, Vadim K. Ivanov, and Andrey V. Solov’yov. Channeling of electrons and positrons in straight and periodically bent diamond(110) crystals. *The European Physical Journal D*, 74(2), 1 2020.
- [26] L. Bandiera et al. Investigation on radiation generated by sub-gev electrons in ultrashort silicon and germanium bent crystals. *Eur. Phys. J. C*, 81(4), 2021.
- [27] V Haurylavets Viktor, V Korol Andrei, B Sushko Gennady, K Ivanov Vadim, and V Solov’yov Andrei. Radiation of high-energy electrons when channeling in the bent silicon and germanium monocrystals. *St. Petersburg Polytechnic University Journal: Physics and Mathematics*, 62(1):33–50, 2023.
- [28] Jiao Y. et al Meng C., He X. Physics design of the heps linac. *Radiat Detect Technol Methods*, 4:497–506, 2020.
- [29] David Krause. Electrons now moving through the superconducting accelerator that will power slac’s x-ray laser. 2023.
- [30] Riccardo Camattari, Vincenzo Guidi, Valerio Bellucci, and Andrea Mazzolari. The ‘quasi-mosaic’ effect in crystals and its applications in modern physics. *Journal of Applied Crystallography*, 48(4):977–989, August 2015.
- [31] Y. M. Ivanov, A. A. Petrunin, and V. V. Skorobogatov. Observation of the elastic quasi-mosaicity effect in bent silicon single crystals. *Jetp Letters*, 81:99–101, 2005.
- [32] V. Guidi, A. Mazzolari, D. De Salvador, and A. Carnera. Silicon crystal for channelling of negatively charged particles. *J. Phys. D: Appl. Phys.*, 42:182005, 2009.
- [33] A. Sytov, L. Bandiera, G. A. P. Cirrone K. Cho, S. Guatelli, V. Haurylavets, V. Ivanchenko S. Hwang, L. Pandola, A. Rosenfeld, and V. Tikhomirov. Geant4 simulation model of electromagnetic processes in oriented crystals for accelerator physics. *J. Korean Phys. Soc.*, 83:132–139, 2023.
- [34] S. Agostinelli et al. Geant4 – A Simulation Toolkit. *Nuclear Instruments and Methods in Physics Research Section A*, 506:250–303, 2003.
- [35] J. Allison et al. Geant4 Developments and Applications. *IEEE Transactions on Nuclear Science*, 53(1):270–278, 2006.
- [36] J. Allison et al. Recent Developments in Geant4. *Nuclear Instruments and Methods in Physics Research Section A*, 835:186–225, 2016.
- [37] V. V. Haurylavets, A. Leukovich, A. Sytov, L. Bandiera, A. Mazzolari, M. Romagnoni, V. Guidi, G. B. Sushko, A. V. Korol, and A. V. Solov’yov. MBN explorer atomistic simulations of 855 MeV electron propagation and radiation emission in oriented silicon bent crystal: theory versus experiment. *The European Physical Journal Plus*, 137(1), 12 2021.
- [38] V.V. Haurylavets, V.K. Ivanov, A.V. Korol, and A.V. Solov’yov. Atomistic modelling of electron propagation and radiation emission in oriented bent ultra-thin Si and Ge crystals. *Nuclear Instruments and Methods in Physics Research Section A Accelerators Spectrometers Detectors and Associated Equipment*, 1058:168917, 11 2023.
- [39] Germán Rojas-Lorenzo, Jesús Rubayo-Soneira, Maykel Márquez-Mijares, Andrei V. Korol, and

- Andrey V. Solov'yov. Multiple scattering of 855 MeV electrons in amorphous and crystalline silicon: Simulations versus experiment. *Nuclear Instruments and Methods in Physics Research Section B Beam Interactions with Materials and Atoms*, 556:165515, 8 2024.
- [40] R. Negrello, L. Bandiera, N. Canale, P. Fedeli, V. Guidi, V.V. Haurylavets, A. Mazzolari, G. Paternò, M. Romagnoni, V.V. Tikhomirov, and A. Sytov. A novel tool for advanced analysis of Geant4 simulations of charged particles interactions in oriented crystals. *Nuclear Instruments and Methods in Physics Research Section A Accelerators Spectrometers Detectors and Associated Equipment*, page 170277, 2 2025.
- [41] H. Backe, P. Kunz, W. Lauth, and A. Rueda. Planar channeling experiments with electrons at the 855 mev mainz microtron mami. *Nuclear Instruments and Methods in Physics Research Section B: Beam Interactions with Materials and Atoms*, 266(17):3835–3851, 2008.
- [42] Valery M. Biryukov, Yuri A. Chesnokov, and Vladilen I. Kotov. *Crystal Channeling and its application at High-Energy accelerators*. 1 1997.
- [43] E. W. Snedden, D. Angal-Kalinin, A. R. Bainbridge, A. D. Brynes, S. R. Buckley, D. J. Dunning, J. R. Henderson, J. K. Jones, K. J. Middleman, T. J. Overton, T. H. Pacey, A. E. Pollard, Y. M. Saveliev, B. J. A. Shepherd, P. H. Williams, M. I. Colling, B. D. Fell, and G. Marshall. Specification and design for full energy beam exploitation of the compact linear accelerator for research and applications. *Phys. Rev. Accel. Beams*, 27:041602, Apr 2024.
- [44] R. Corsini, W. Farabolini, P. Korysko, A. Malyzhenkov, V. Rieker, and K. N. Sjobak. Status of the CLEAR User Facility at CERN and its Experiments. In *Proc. LINAC'22*, pages 753–757, 2022.
- [45] T. Vinatier, R. Assmann, F. Burkart, H. Dinter, S. M. Jaster-Merz, M. Kellermeier, W. Kuropka, F. Mayet, B. Stacey, and C. Bruni. Characterization of relativistic electron bunch duration and traveling wave structure phase velocity based on momentum spectra measurements. *Phys. Rev. Accel. Beams*, 27, 2024.
- [46] Sources for plasma accelerators and radiation compton with laser and beam (sparc_lab).
- [47] P. Villanueva-Perez, H. Fleckenstein, M. Prasciolu, K. T. Murray, M. Domaracký, K. Gregorič, V. Mariani, L. Gelisio, M. Kuhn, J. Hannappel, O. Yefanov, N. Ivanov, I. Sarrou, D. Pennicard, J. Becker, M. von Zimmermann, O. Gutowski, A.-C. Dippel, H. N. Chapman, and S. Bajt. Scanning compton x-ray microscopy. *Opt. Lett.*, 46(8):1920–1923, Apr 2021.
- [48] Khabaz R Adeli S. Determination of the protective properties of materials for industrial x-ray generators having a continuous energy spectrum. *Eur. Phys. J. Plus*, 137:1064, 2022.
- [49] R. Chehab, T. Flavio, R. Rossmanith, and A. Wagner. Positron-production experiment in tungsten crystal using 4 and 8 gev electron beams. In *Proceedings of the European Particle Accelerator Conference (EPAC)*, pages 736–738, 2002.
- [50] Xuan Gao, Peng Zhang, Jia Li, Wang Mao, Zifang Guo, Jiaolong Li, Yanshi Zhang, Jialiang Chen, Liusi Sheng, and Mingzhang Lin. Production of 99Mo via photoneutron reaction using a 50 MeV electron linear accelerator. *Journal of Radioanalytical and Nuclear Chemistry*, 332(8):3037–3045, 7 2023.
- [51] V.G. Baryshevsky, I.Ya. Dubovskaya, and A.O. Grubich. Generation of γ -quanta by channeled particles in the presence of a variable external field. *Physics Letters A*, 77(1):61–64, 1980.
- [52] A.V. Korol, A.V. Solov'yov, and W. Greiner. Coherent radiation of an ultra-relativistic charged particle channeled in a periodically bent crystal. *Journal of Physics G: Nuclear and Particle Physics*, 24:L45–L53, 1998.
- [53] V.G. Baryshevsky and V.V. Tikhomirov. Crystal undulators: from the prediction to the mature simulations. *Nuclear Instruments and Methods in Physics Research Section B: Beam Interactions with Materials and Atoms*, 309:30–36, 2013.
- [54] A. Kostyuk and U. et al. Uggerhøj. Experimental realization of a new type of crystalline undulator. *Physical Review Letters*, 112(25):254801, 2014.
- [55] Andrei V Korol and Andrey V Solov'yov. Crystal-based intensive gamma-ray light sources. *The European Physical Journal D*, 74:1–17, 2020.
- [56] Victor Tikhomirov. Multiple volume reflection from different planes inside one bent crystal. *Physics Letters B*, 655(5-6):217–222, 10 2007.
- [57] V. Guidi, A. Mazzolari, and V.V. Tikhomirov. Planar channeling in a periodically bent crystal: Analytical and numerical study. *Journal of Applied Physics*, 107:114908, 2010.
- [58] V. Guidi, L. Bandiera, and V. Tikhomirov. Radiation generated by single and multiple volume reflection of ultrarelativistic electrons and positrons in bent crystals. *Physical Review A*, 86(4):042903, 2012.

- [59] L. Bandiera, V. Guidi, and V. Tikhomirov. Broad and intense radiation accompanying multiple volume reflection of ultrarelativistic electrons in a bent crystal. *Physical Review Letters*, 111(25):255502, 2013.